

RESEARCH

Open Access



Low-dose pleiotropic radiosensitive nanoformulations for three-pronged radiochemotherapy of hypoxic brain glioblastoma under BOLD/DWI monitoring

Fangshi Zhao^{1†}, Xiaoyi Wang^{2†}, Wei Zhu^{3†}, Dongju Zhao¹, Caihua Ye¹, Yanyan Guo^{2*} and Yan Dou^{1*}

[†]Fangshi Zhao, Xiaoyi Wang, and Wei Zhu contributed equally to this work

*Correspondence: graveyanyan@163.com; douyan@tmu.edu.cn

¹ Department of Radiology and Tianjin Key Laboratory of Functional Imaging, Tianjin Medical University General Hospital, Tianjin 300052, China
² Department of Ultrasound and Department of Radiation Oncology, The Second Hospital of Tianjin Medical University, Tianjin 300211, China
³ Tianjin Huanhu Hospital, Tianjin 300350, China

Abstract

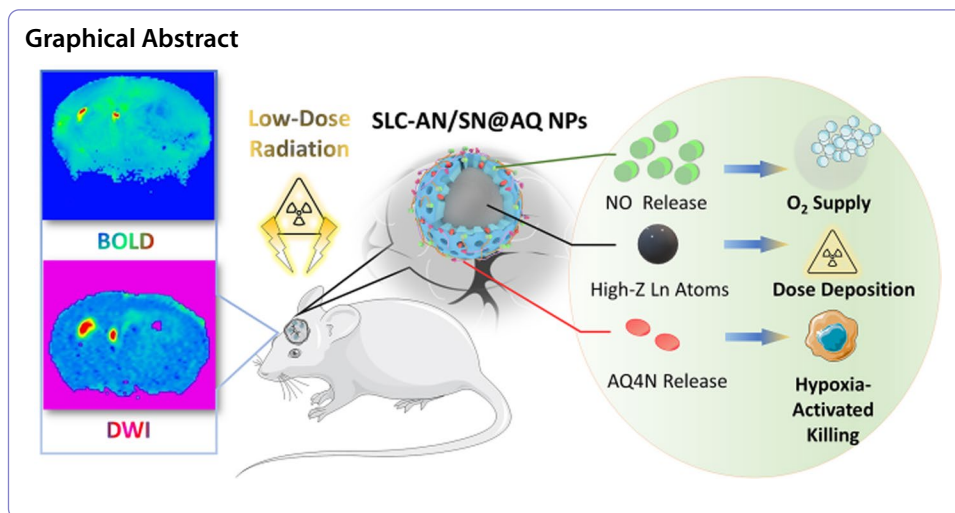
Background: Hypoxia-mediated radioresistance is the main obstacle to the successful treatment of glioblastoma (GBM). Enhancing hypoxic radiosensitivity and alleviating tumor hypoxia are both effective means to improve therapeutic efficacy, and the combination of the two is highly desirable and meaningful.

Results: Herein, we construct a low-dose pleiotropic radiosensitive nanoformulation consisting of a high-Z atomic nanocrystal core and mesoporous silica shell, surface-modified with angiopep-2 (ANG) peptide and loaded with nitric oxide (NO) donor and hypoxia-activated prodrug (AQ4N). Benefiting from ANG-mediated transcytosis, this nanoformulation can efficiently cross the BBB and accumulate preferentially in the brain. Low-dose radiation triggers this nanoformulation to exert a three-pronged synergistic therapeutic effect through high-Z-atom-dependent dose deposition enhancement, NO-mediated hypoxia relief, and AQ4N-induced hypoxia-selective killing, thereby significantly inhibiting GBM in situ growth while prolonging survival and maintaining stable body weight in the glioma-bearing mice. Meanwhile, the proposed in vivo 9.4 T BOLD/DWI can realize real-time dynamic assessment of local oxygen supply and radiosensitivity to monitor the therapeutic response of GBM.

Conclusions: This work provides a promising alternative for hypoxia-specific GBM-targeted comprehensive therapy, noninvasive monitoring, and precise prognosis.

Keywords: Nanomedicine, Glioblastoma, Tumor hypoxia, Radiochemotherapy, Hypoxia-activated therapy, Nitric oxide, 9.4 T BOLD/DWI imaging





Introduction

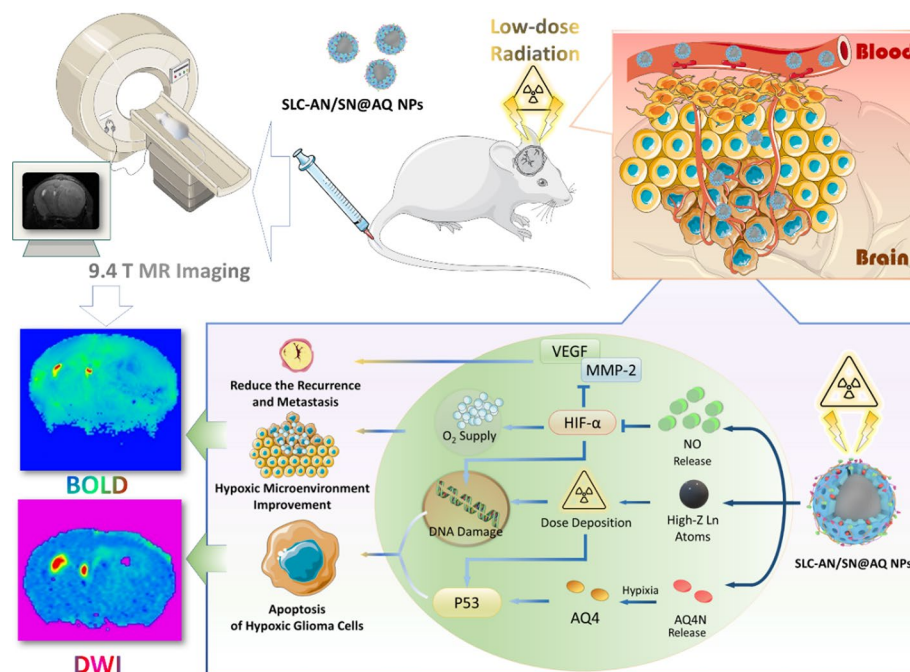
Glioblastoma (GBM) is the most common and aggressive primary malignant brain tumor with high mortality and short survival (Omuro and DeAngelis 2013; Gregory et al. 2020; Lu et al. 2022). Surgery combined with radiotherapy (RT) and chemotherapy is currently the standard treatment for GBM (Du et al. 2020; Wen et al. 2020; Dong et al. 2021). However, due to infiltrative growth and high heterogeneity, GBM is poorly curable and highly prone to recurrence (Tan et al. 2020a). In addition to incomplete surgical resection, these adverse outcomes are largely attributed to the highly hypoxic microenvironment of gliomas (Kizaka-Kondoh et al. 2003). Tumor hypoxia not only induces tumor development and metastasis but also severely reduces the responsiveness of tumor tissue to RT and chemotherapy, ultimately leading to the failure of glioma treatment (Fu et al. 2021; Chedeville and Madureira 2021; Shi et al. 2021). Therefore, enhancing the hypoxic sensitivity of glioma cells and improving the hypoxic microenvironment are both effective means to improve the efficacy of glioma, and the combination of the two is very desirable and meaningful.

The advent of radiosensitizers provides a potential way to enhance local radiation damage, typically high-Z elements that can strongly increase local radiation energy deposition when accumulated in tumors (Dong et al. 2021; Zhou et al. 2022; Li et al. 2021; Choi et al. 2020). Among them, nanomaterials composed of rare earth elements such as gadolinium (Gd) have become popular due to their excellent radiosensitivity, chemical stability, and low biotoxicity (Bulin et al. 2020; Shen et al. 2020; Stasio et al. 2006). Although these radiosensitizers rely on the interaction between atoms and X-rays rather than oxygen, the efficiency of this effect generally depends on the dose of X-rays (Lu et al. 2019). The high doses required to achieve the ideal RT effect of GBM will bring obvious toxic and side effects to normal brain tissues, so it is clinically valuable to achieve low-dose radiosensitization. Bioreductive drugs such as banoxantrone (AQ4N) are nontoxic chemotherapeutic prodrugs, which can be converted into toxic AQ4 molecules under hypoxia to selectively kill hypoxic tumor cells (Feng et al. 2017; Shen et al. 2018; Wang et al. 2021). Therefore, AQ4N chemotherapy combined with RT is beneficial to achieve satisfactory RT efficacy of GBM at lower radiation doses, while reducing undesired radiation toxicity.

Enhancing the local oxygen supply in gliomas is another important way to improve the RT efficacy of GBM. Clinical hyperbaric oxygen therapy can rapidly increase blood oxygen concentration in the whole body, but it lacks tumor specificity and carries the risk of hyperoxia toxicity (Daruwalla and Christophi 2006). Although oxygen delivery systems have been developed, peroxygenation induced in this manner avoids tumor metastasis but may also exacerbate primary tumor growth (Song et al. 2016; Zou et al. 2021). Nitric oxide (NO) has received extensive attention in recent years for its unique anticancer properties (Cao et al. 2020; Xu et al. 2020). The targeted release of NO in tumor sites can not only normalize the distorted tumor vascular structure and function to restore normal tumor oxygen supply, but also promote RT and chemotherapy-induced apoptosis (Zhang et al. 2020; Sung et al. 2019). Given that the efficiency of intracerebral delivery is limited by the blood–brain barrier (BBB), low-density lipoprotein receptor-related protein 1 (LRP-1), which is overexpressed on both BBB and glioma cells, has emerged as a key target for efficient glioma delivery (Jiang et al. 2018; Tian et al. 2015).

Nevertheless, inaccurate prognostic monitoring fails to provide an effective time window for adjusting individual GBM treatment regimens. Noninvasive magnetic resonance imaging (MRI) plays an increasingly prominent role in the efficacy evaluation and monitoring of gliomas, providing high spatial and soft tissue resolution of the brain at high field strengths (Xie et al. 2021; Compter et al. 2016). Conventional contrast-enhanced imaging only visualizes brain anatomy and is difficult to distinguish and track the infiltrating high-grade gliomas (Xie et al. 2021). In contrast, functional imaging modality (fMRI) can provide rich anatomical and functional information, allowing more sensitive and accurate dynamic observations of glioma treatment outcomes (Huang et al. 2020). Among them, blood oxygenation level-dependent (BOLD) fMRI depends on paramagnetic deoxyhemoglobin content, which increases under hypoxia, resulting in decreased $T2^*$ signal, and can be used to assess the oxygenation status of glioma in real time (Toth et al. 2013; Iranmahboob et al. 2016). Diffusion-weighted imaging (DWI) relies on the diffusion motion of water molecules in living tissue and its associated apparent diffusion coefficient (ADC) is inversely proportional to tumor cell density, which can be used to sensitively evaluate glioma killing effects (Liu et al. 2017a; Calli et al. 2006).

Herein, we presented a low-dose pleiotropic radiosensitive nanoformulation (SLC-AN/SN@AQ NPs) by encapsulating AQ4N into the cavity of mesoporous silica coating on $\text{NaGdF}_4:\text{Eu}^{3+}$ (SLC) nanocrystals with surface modification of the NO donor S-nitrosothiol (SNO) and the LRP ligand angiopep-2 (ANG). Benefiting from ANG-mediated efficient brain delivery, this nanoformulation realized the three-pronged hypoxic radiosensitization under low-dose radiation by combining high-Z-atom (Gd and Eu)-enhanced physical dose deposition, NO-mediated hypoxia relief, and AQ4N-induced hypoxia-activated chemotherapy (Scheme 1). In vivo 9.4 T BOLD/DWI dynamically assessed this therapeutic strategy by monitoring local oxygenation status and treatment response in gliomas. This study provided a promising candidate to comprehensively overcome radioresistance in hypoxic gliomas monitored by fMRI for future clinical translation.



Scheme 1 The schematic illustration of SLC-AN/SN@AQ NPs for three-pronged hypoxic radiosensitization of brain gliomas under BOLD/DWI monitoring. Benefiting from angioprep-2-mediated brain delivery, this nanoformulation enables an efficient combination of high Z-atom-dependent dose deposition enhancement, NO-mediated hypoxia relief, and AQ4N-induced hypoxia-activated chemotherapy under low-dose radiation. Meanwhile, in vivo 9.4 T BOLD/DWI realizes real-time dynamic assessment of local oxygen supply and treatment response of brain gliomas

Materials and methods

Materials

All chemicals were purchased from Sigma-Aldrich and used without any purification. Angioprep-2 (ANG, TFFYGGSRGKRNNFKTEEYC) was synthesized by the Chinese Peptide Company. Banoxantrone dihydrochloride (AQ4N) was purchased from Abcam. Bicinchoninic acid (BCA) protein assay kit and nitric oxide detection kit (DAF-FM DA) were obtained from Beyotime Biotechnology Co., Ltd. Cell Counting Kit-8 (CCK-8) assay kit was purchased from New Cell & Molecular Biotech Co., Ltd. Calcein-AM and PI were purchased from Solarbio Science & Technology Co., Ltd. Comet assay kit was purchased from AmyJet Scientific, Inc. Cy5.5 NHS Ester was purchased from Thermo Fisher Scientific, Inc. Hypoxyprobe-1 kit (pimonidazole hydrochloride) was purchased from Hypoxyprobe, Inc. Anti-p53, anti-HIF-1 α , anti-VEGF, and anti-MMP-2 antibodies were purchased from Abcam. Ultrapure water was obtained from a Milli-Q ultrapure water system.

Preparation of SLC-AN/SN@AQ NPs

Gadolinium chloride (0.354 M, 2 mL), europium chloride (0.036 M, 2 mL), and sodium citrate (0.3 M, 8 mL) were mixed, then sodium fluoride (1.2 M, 5 mL) was dripped and heated at 210 °C for 1.5 h. The prepared NPs were mixed with cetyltrimethyl ammonium chloride (0.294 M, 10 mL) and triethanolamine (0.034 M, 2 mL), and then tetraethyl

orthosilicate (150 μL) was added and heated at 80 $^{\circ}\text{C}$ for 1 h to obtain SLC NPs. Subsequently, SLC NPs were suspended in ethanol, and 3-aminopropyltriethoxysilane (17.5 μL), 3-mercaptopropyltrimethoxysilane (20 μL), and $\text{NH}_3\cdot\text{H}_2\text{O}$ (25–28%, 65 μL) were successively added for overnight stirring to obtain amine/sulfhydryl-functionalized SLC NPs. Next, ANG (6.2 μmol) was incubated with EDC (256 μmol) and NHS (420 μmol) at room temperature for 30 min, and 0.1 μmol NPs were added for 24 h slow stirring to obtain SLC-AN NPs. Then, the NPs were suspended in methanol/toluene ($v/v=4:1$, 10 mL) and stirred with *t*-butyl nitrite (0.88 mL) in the dark for 24 h to obtain SLC-AN/SN NPs. Finally, AQ4N solution (19.3 μmol) was mixed with SLC-AN/SN NPs for overnight stirring at room temperature to obtain SLC-AN/SN@AQ NPs. The resulting NPs at each step were centrifugally washed with deionized water at least three times before proceeding to the next step.

Characterization

Transmission electron microscopy (TEM, HT7700, Hitachi, Japan) was conducted to characterize the morphologies of NPs. Dynamic light scattering (DLS) sizes and zeta potentials were measured using a Zetasizer Nano system (Malvern Instruments Ltd., UK). Nitrogen adsorption–desorption isotherms were measured to assess the mesoporous performance of NPs using a TriStar II 3020 analyzer (Micromeritics Instrument, USA). Brunauer–Emmett–Teller (BET) and Barrett–Joyner–Halenda (BJH) methods were respectively used to calculate the surface area and pore-size distribution. UV–vis–NIR absorption spectra were acquired using a UV-3600 Plus Shimadzu spectrophotometer (Shimadzu, Co., Japan). The content of conjugated ANG on NPs was determined by the BCA protein assay kit.

NO production and AQ4N release in vitro

NO production in vitro was quantified using the Nitric Oxide Assay Kit. SLC-AN NPs, SLC-AN/SN NPs, and SLC-AN/SN@AQ NPs suspensions were irradiated with X-ray radiation at 1 Gy using a clinical electron linear accelerator (ELEKTA Presice, England) with 6 MeV at 200 cGy/min, and then reacted with Griess reagent to determine the absorbance at 540 nm using a multifunctional microplate reader (Thermo Scientific, USA) to calculate NO concentration (μM). To assess the drug release behavior of AQ4N in vitro, SLC-AN/SN@AQ NPs were encapsulated in dialysis bags (MWCO 3500) and placed into phosphate buffer (pH 7.4) for gentle shaking at 37 $^{\circ}\text{C}$ at 100 rpm. At certain time intervals, 200 μL incubation medium was withdrawn and tested the characteristic UV–vis absorbance of AQ4N at 610 nm, and then poured back into the medium. The cumulative release percentage of AQ4N from SLC-AN/SN@AQ NPs was calculated as follows: $\text{Wrel} \times 100\% / \text{Wini}$ (Wrel: the released amount, Wini: the initial amount). To assess the release behavior under RT, SLC-AN/SN@AQ NPs suspensions were exposed to X-ray radiation at 1 Gy, and the above dialysis analysis was performed.

Cell viability

Human glioma cells U87MG were obtained from the School of Basic Medicine Sciences of Tianjin Medical University and seeded in a 96-well plate at 5×10^3 cells per well for 24 h normoxic (21% O_2) incubation at 37 $^{\circ}\text{C}$ with 5% CO_2 . Then, the U87MG cells were

incubated with SLC-AN NPs, SLC-AN/SN NPs, and SLC-AN/SN@AQ NPs at various concentrations in normoxic or hypoxic (2% O₂) condition for 24 h. After being replaced with the fresh medium, the cells were cultured for another 24 h in normoxic conditions. Cell Counting Kit-8 (CCK-8) solution was then added and cultured at 37 °C for 4 h. The absorbance at 450 nm was recorded using a multifunctional microplate reader to determine the cell viabilities.

Flow cytometry analysis

U87MG cells were seeded at 2×10^5 cells per well in 6-well plates for 24 h culture and incubated with SLC-AN NPs, SLC-AN/SN NPs, and SLC-AN/SN@AQ NPs at 10 µg/mL in normoxic or hypoxic condition for another 24 h. After being exposed to X-ray radiation at 1 Gy, the cell culture medium was replaced with the NO probe solution (3-amino-4-aminomethyl-2',7'-difluorescein diacetate, DAF-FM DA) for 30 min culture at 37 °C. Then, the cells were washed with deionized water at least three times and collected to detect the fluorescent intensity of produced NO using flow cytometry (BD FACSCalibur, USA).

Colony formation assay

Human glioma cells U87MG and U251 were obtained from the School of Basic Medicine Sciences of Tianjin Medical University and respectively seeded at 5×10^4 cells per well in 6-well plates and cultured for 24 h. After incubated with SLC-AN NPs, SLC-AN/SN NPs, and SLC-AN/SN@AQ NPs at 10 µg/mL in normoxic or hypoxic conditions for 24 h, the cells were exposed to X-ray radiation at 1 Gy and then transferred to a new six-well plate for 7 days in normoxic condition. Then, the cells were fixed with formalin and stained with 0.5% crystal violet. Colonies containing more than 50 cells were counted to calculate the survival fractions (SF).

Comet assay

After being exposed to X-ray radiation at 1 Gy, NPs-treated U87MG and U251 cells were respectively prepared into single-cell suspensions at 2×10^4 /mL and then immobilized in a bed of low melting point agarose on a specially treated Comet Slide. Following gentle cell lysis at 4 °C overnight, the slides were gently washed and immersed in an alkaline DNA precipitation solution for 30 min. Then, the electrophoresis was performed for 20 min under 20 V and 200 mA. The slides were dried and stained in ethidium bromide for 30 min. The cells with comet tails were observed by an inverted fluorescence microscope (Olympus, Japan) and the tail length was analyzed using CASP software (Poland).

Calcein AM/PI dual staining

U87MG and U251 cells were respectively seeded at 4×10^5 cells per well in 24-well plates and cultured overnight. SLC-AN NPs, SLC-AN/SN NPs, and SLC-AN/SN@AQ NPs at 10 µg/mL were incubated with U87MG cells for 12 h and then exposed to X-ray radiation at 1 Gy. The cells without NPs treatment under X-ray radiation were used as contrast. Then, the cells were stained with Calcein-AM and PI and observed under

an inverted fluorescence microscope. The relative PI level was analyzed using Image J software.

Transwell migration assay

To construct the BBB in vitro model, bEnd.3 cells were seeded at 8×10^4 cells/well on 24-well transwells with permeable polyester membrane inserts (Corning). After two-week cultures, the integrity of bEnd.3 monolayer was assessed by measuring the transepithelial electrical resistance (TEER) value using an epithelial voltohmmeter (Millicell-RES, Millipore, USA). The bEnd.3 cells with a TEER value of above $150 \Omega \cdot \text{cm}^2$ were selected for performing in vitro BBB transcytosis. SLC-AN/SN@AQ NPs were introduced into the apical chamber at $100 \mu\text{g}/\text{mL}$ and the TEER value was measured during 24 h incubation at 37°C . Then, the cells in the lower chamber were collected to detect the Ln (Gd + Eu) content by inductively coupled plasma optical emission spectrometry (ICP-OES). Non-ANG modified NPs were used as contrast. In the blocking study, ANG was added at $5 \text{ mg}/\text{mL}$ to the apical chamber for 3 h before the incubation of NPs, followed by the above-mentioned steps.

Animals and brain glioma orthotopic xenograft model

All animal experiments were performed according to Tianjin Medical University Guidelines for Animal Research and were approved by Tianjin Medical University Animal Care and Use Committee. BALB/c-nude mice (female, 6–8 weeks old, 20 g) were purchased from Vital River Laboratory Animal Technology Co., Ltd. (Beijing, China). 5×10^5 U87MG cells were implanted into the right lateral ventricle of the mice by using a stereotactic fixation instrument. After 14 days, the glioma orthotopic xenograft model was successfully established, namely the glioma-bearing mice.

Pharmacokinetics and biodistribution studies

The glioma-bearing mice were intravenously injected with SLC-AN/SN@AQ NPs at $25 \text{ mg}/\text{kg}$, and the plasma samples and brain tissues were collected 6 h, 12 h, 24 h, and 48 h after the injection. After dissolved in digestive chloroazotic acid ($\text{HNO}_3/\text{HCl} = 3/1$), the amount of lanthanides (Ln: Gd + Eu) was quantified by ICP-OES. At 24 h post-injection, the brain tissues and major organs (heart, liver, spleen, lung, kidney) were harvested for digestion and the quantitative biodistributions of Ln were measured by inductively coupled plasma optical emission spectrometry (ICP-OES). Then, SLC-AN/SN@AQ NPs were pre-labeled with Cy5.5, and then intravenously injected into the glioma-bearing mice. At 24 h post-injection, the images of the living mice were taken by IVIS Imaging System (IVIS Spectrum, PerkinElmer, USA). Then, the brain tissues and major organs were harvested for ex vivo imaging, and the fluorescence intensity of the Cy5.5 signal was measured by IVIS Image Software. In these experiments, SLC-SN@AQ NPs were used as a contrast.

9.4 T MRI scanning in vivo

The glioma-bearing mice were divided into five groups randomly. The experimental group was intravenously injected with 0.9% NaCl, SLC-AN NPs, SLC-AN/SN NPs, and SLC-AN/SN@AQ NPs at $25 \text{ mg}/\text{kg}$, respectively, and then subjected to 1 Gy on a clinical

electron linear accelerator with 6 MeV at 200 cGy min⁻¹ using a 2 cm × 2 cm radiation field under a source-to-skin distance (SSD) of 80 cm to cover the entire right brain containing glioma region of interest (ROI). The group was only intravenously injected with 0.9% NaCl without radiotherapy as control. Before and 7, 14 days after radiation, in vivo MR images of mice were acquired by a 9.4 T MRI scanner (Bruker BioSpec 94/30 USR, Germany) with the following scan parameters: (1) T2-weighted sequence: TR = 2900 ms, TE = 33 ms, slice thickness = 0.5 mm, the field of view (FOV) = 20 mm × 20 mm, 15 contiguous slices. Imaging tumor volumes were calculated as the sum of the manually drawn glioma ROI multiplied by the slice thickness for each slice. (2) BOLD sequence: TR = 705 ms, TE = 4 ms, slice thickness = 0.5 mm, FOV = 15 mm × 15 mm, Flip Angle = 25°, 15 contiguous slices. T2* values were calculated as the mean value of the glioma ROI for all slices. (3) DWI sequence: SE-EPI sequence. TR = 3000 ms, TE = 30 ms, slice thickness = 0.5 mm, FOV = 18 mm × 18 mm, Flip Angle = 90°, 20 contiguous slices. ADC values were calculated with reference to images with b values of 1000 s mm⁻² and 0 s mm⁻².

Anti-glioma efficacy in vivo

24 h after intravenous administration of SLC-AN NPs, SLC-AN/SN NPs, and SLC-AN/SN@AQ NPs at 25 mg/kg, the brains of the glioma-bearing mice were exposed to X-ray radiation at 1 Gy. During 14 days of treatments, the body weights of the glioma-bearing mice were measured every 3 days. After 14 days, the glioma-bearing brain tissues were removed and fixed for hematoxylin and eosin (H&E) and terminal deoxynucleotidyl transferase dUTP nick end labeling (TUNEL) staining. In addition, other brain slices were prepared and blocked with normal goat serum. Then, the slices were incubated with the primary antibodies including rabbit monoclonal anti-p53, anti-HIF-1 α , anti-VEGF, and anti-MMP-2 antibodies. Biotin-conjugated goat anti-rabbit IgG (secondary antibody, Abcam) was subsequently added, followed by 3,3'-diaminobenzidine (DAB) staining and hematoxylin counterstaining successively. Immunohistochemical images were acquired using a fluorescence microscope (BX51T-PHD-J11, Olympus). The survival rate of mice was measured as the percentage of the number of mice alive at indicated time points to the total number of original mice.

In vivo biosafety analysis

After 14 days of treatments, routine blood and serum biochemistry were detected by blood samples collected from the retro-orbital plexus of the glioma-bearing mice. Then, the mice were killed, and the glioma-free left brain tissues and major organs including heart, liver, spleen, lung, and kidney were collected for hematoxylin–eosin (H&E) staining.

Statistical analysis

Data are presented as means \pm standard deviation (SD) and significance was analyzed by a Student's t-test (two-tailed) using OriginPro (OriginLab Corporation, USA). * $p < 0.05$, ** $p < 0.01$, *** $p < 0.001$.

Results and discussion

Preparation and characterization of SLC-AN/SN@AQ NPs

In this nanoformulation, $\text{NaGdF}_4:\text{Eu}^{3+}$ (SLC) nanocrystals served as high-Z cores for physical dose deposition, and mesoporous silica shells were surface modified with amino and sulfhydryl groups to conjugate ANG and SNO for BBB crossing and glioma targeting as well as radiation-responsive NO release, respectively. AQ4N was finally loaded into the cavity of the mesoporous silica shell to obtain SLC-AN/SN@AQ NPs (Additional file 1: Fig. S1). As shown in the TEM image (Fig. 1A), SLC-AN/SN@AQ NPs exhibited a core-shell structure with a core of ~ 93 nm and a shell of ~ 25 nm. DLS results showed that the average particle diameter after each step of surface modification increased to varied extents, and the final particle diameter of SLC-AN/SN@AQ NPs was ~ 142 nm with uniform particle size distribution (Fig. 1B). Nitrogen adsorption-desorption isotherms further confirmed the mesoporous structure of the shells, characterized by a BET surface area of $361 \text{ m}^2 \text{ g}^{-1}$ and a BJH pore size of 4.3 nm (Fig. 1C).

ANG conjugation positively shifted the zeta potential of SLC NPs from -8.5 mV to -2.4 mV, further SNO conjugation shifted it negatively to -5.6 mV, and the final surface charge of this nanoformulation after AQ4N loading was about -5.8 mV. BCA protein assay was used to determine the content of ANG conjugated on the NPs, which was calculated to be $96.7 \mu\text{g}/\text{mg}$ (Additional file 1: Fig. S2), confirming the successful surface modification of ANG on the NPs. UV-vis-NIR spectra showed that SLC-AN/SN@AQ NPs exhibited the obvious characteristic absorption bands for SNO at 350–380 nm and characteristic absorbance peak for AQ4N at 610 nm, which confirmed the successful SNO conjugation and AQ4N loading (Fig. 1D). The loading content (DLC) of AQ4N in SLC-AN/SN@AQ NPs was determined to be 8.79%. In addition, no significant change in DLS particle size was observed within 14 days after incubation with SLC-AN/SN@AQ NPs in different biological media, showing excellent particle size stability (Additional file 1: Fig. S3).

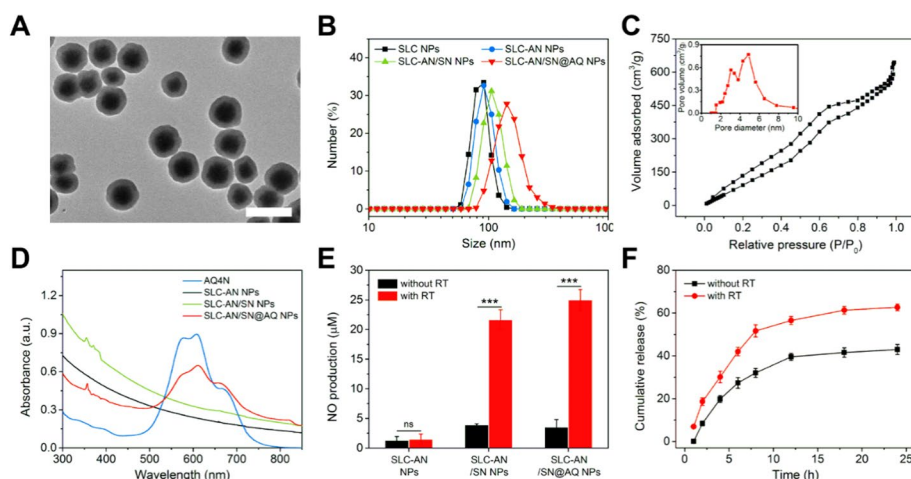


Fig. 1 Characterization of SLC-AN/SN@AQ NPs. **A** TEM image. Scale bar = 200 nm. **B** DLS size distributions. **C, D** UV-vis-NIR absorption spectra. **E** NO produced by different NPs with or without X-ray radiation. **F** Cumulative release profile of AQ4N from SLC-AN/SN@AQ NPs with or without X-ray radiation. Radiation dose: 1 Gy

Next, we studied the radiation-responsive NO release by SLC-AN/SN@AQ NPs using a nitrate/nitrite assay kit. SLC-AN NPs did not produce NO with or without low-dose X-ray radiation (1 Gy), while all SNO-conjugated NPs produced a large amount of NO only under radiation (Fig. 1E). The above results confirmed the specific NO release induced by low-dose radiation and further validated the successful conjugation of SNO. Furthermore, we monitored the release profiles of AQ4N from SLC-AN/SN@AQ NPs. Without radiation, ~42% AQ4N was released from NPs after 24 h incubation in PBS. In contrast, 1 Gy radiation promoted the release behavior of AQ4N, and the cumulative drug release was ~63% after 24 h (Fig. 1F). This might be due to the decrease of a steric hindrance after the release of NO by the chemical bond breaking of SNO, which accelerated the release of AQ4N.

Low-dose synergistic radiosensitive effect on hypoxic U87MG cells

To evaluate the hypoxic radiosensitive effect, human glioma cells U87MG were incubated with SLC-AN/SN@AQ NPs under both hypoxic and normoxic conditions, followed by low-dose X-ray radiation (1 Gy). To construct the in vitro cell model of brain gliomas, the U87MG cell line was selected in this work because it is the commonly used human high-grade glioma cell line in many nanomedical studies for the treatment of mouse brain gliomas (Brighi et al. 2020; Zhang et al. 2021; Lam et al. 2018). Furthermore, as previously reported, most of the oxygen concentrations in brain gliomas under hypoxia fluctuate between 0.5% and 2.5%, so the 2% oxygen level that has been extensively adopted in many nanomedicine-related studies was selected to construct the in vitro hypoxic glioma model in this work (Bar et al. 2010; Liu et al. 2017b; Tan et al. 2020b).

For all studied NPs, there was no significant effect on cell viability at concentrations up to 100 µg/mL under both hypoxic and normoxic conditions (Additional file 1: Fig. S4), indicating low cytotoxicity. Then, radiation-induced NO production was analyzed in U87MG cells treated with SLC-AN/SN@AQ NPs by quantitatively detecting DAF-FM-labeled fluorescence through flow cytometry. It was shown that only SNO-conjugated NP treatment elicited high intracellular NO production under either normoxia or hypoxia, compared to almost no NO production after low-dose RT alone and SLC-AN NP treatment, regardless of normoxia or hypoxia. (Fig. 2A and Additional file 1: Fig. S5). Hypoxia-activated cytotoxicity of SLC-AN/SN@AQ NPs was then detected using the standard CCK-8 assay. Compared with the limited killing of normoxic U87MG cells by SLC-AN/SN@AQ NPs, their half-maximal inhibitory concentration (IC₅₀) values against hypoxic cells dropped sharply to about 10 µg/mL (Fig. 2B). These results demonstrated that this nanoformulation could trigger excellent radiation-induced NO release and selective chemo-killing under hypoxia.

The low-dose synergistic radiosensitive effect induced by this nanoformulation on hypoxic U87MG cells was evaluated by the survival fractions (SF) using colony formation assay (Fig. 2C). The SF values of all cells after low-dose RT alone remained still high above 85%, and SLC-AN NPs showed slightly lower SF values in normoxic cells than in hypoxic cells. This phenomenon illustrated the huge limitation of hypoxia on low-dose RT and low-dose physical radiosensitization (Song et al. 2017).

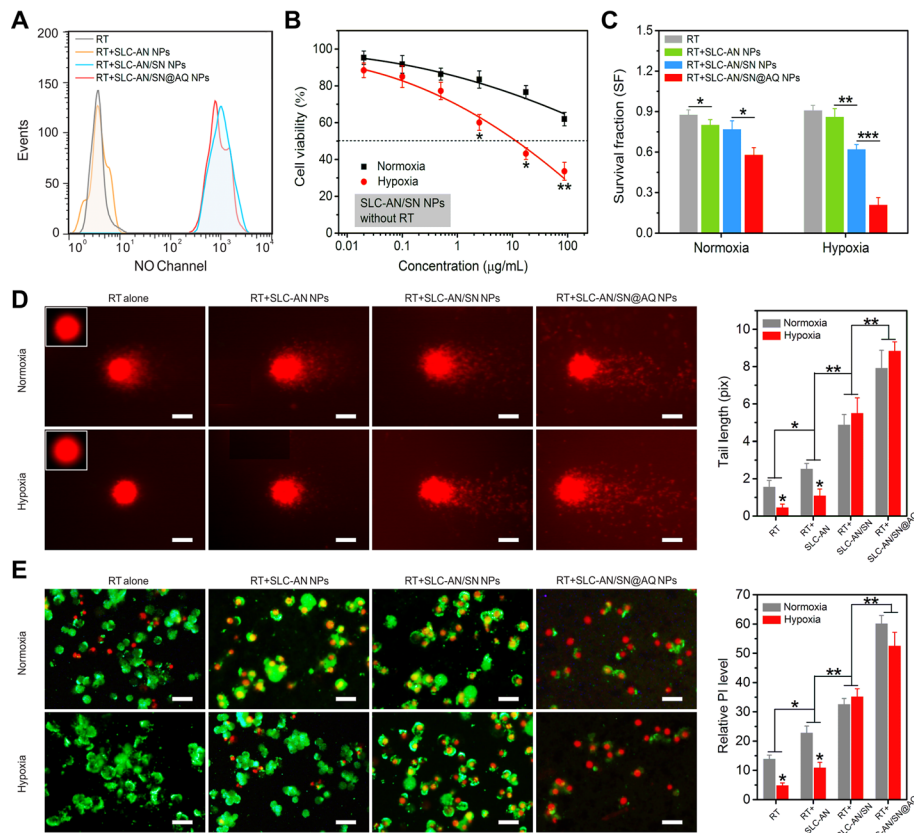


Fig. 2 Low-dose synergistic radiosensitive effect on hypoxic U87MG cells. **A** NO production in cells under radiation under hypoxic conditions. **B** Cytotoxicity of SLC-AN/SN@AQ NPs to U87MG cells under normoxic and hypoxic conditions measured by CCK-8 assay. **C** Multi-effect synergistic effect evaluated by colony formation assay. **D** DNA damage assessed by Comet assay. Insert: the control group. **E** Live (Green) and dead (Red) cells labeled by Calcein AM/PI dual staining. Radiation dose: 1 Gy

The radiation damage to hypoxic cells was significantly greater than that of normoxic cells under high concentrations of NO produced, showing the enhancement effect of NO on hypoxic radiosensitization. Further AQ4N release resulted in the lowest SF values, especially in hypoxic cells, indicating that SLC-AN/SN@AQ NPs exhibited the most potent inhibition of hypoxic glioma cell proliferation under low-dose radiation by combining the therapeutic effects of NO and AQ4N.

Potential DNA damage induced by this synergistic hypoxic radiosensitization was subsequently detected by the comet assay. It was found that both low-dose RT alone and RT + SLC-AN NPs groups induced only a small amount of free DNA fragments in normoxic cells, and almost none were observed in hypoxic cells. RT + SLC-AN/SN NPs group exhibited a longer comet-like appearance with no significant difference between hypoxic and normoxic conditions, suggesting that NO production during low-dose RT could accelerate DNA damage in hypoxic cells. The longest comet tails were observed in the RT + SLC-AN/SN@AQ NPs group and were more pronounced in hypoxic cells than in normoxic cells, attributed to the selective hypoxic killing effect of AQ4N (Fig. 2D). As shown in Calcein-AM/PI dual staining, only SNO-containing NP sensitization treatment increased the radiation killing effect on hypoxic

cells to the same level as that of normoxic cells, while SLC-AN/SN@AQ NP sensitization treatment caused almost complete cell death under both normoxic and hypoxic conditions (Fig. 2E). Taken together, these results demonstrated that SLC-AN/SN@AQ NPs could induce efficient radiation killing on hypoxic glioma cells by combining dose deposition enhancement, NO-mediated sensitization, and hypoxia-activated chemotherapy.

Therapeutic response of U87MG and U251 cell lines

To preliminarily evaluate the consistency of the efficacy of this nanoformulation against different GBM cell lines, we first conducted a screening analysis of journal articles in the field of nanomedicine to identify the cell lines most commonly used for nanoparticle-based RT of GBM. The Clarivate Analytics Web of Science was searched with “nano” and “treatment” as the keywords for related reports in the last 3 years (2020–2022), and then filtrated with “glioma” to yield 559 papers. After removing review articles and conference abstracts, there were 39 papers involving RT, among which 32 papers involved in vivo studies (Fig. 3A). Of these 32 reports, 12 articles used U87MG cells and 7 articles used U251 cells for in vitro and in vivo modeling, both of which are the most common human malignant GBM cell lines, while the remaining few articles used mouse (GL261) or rat (C6 and F98) glioma cell lines (Fig. 3A). Since human GBM cell lines are more conducive to future preclinical studies, U87MG and U251 cells that accounted for more than 50% of nanomedical studies are worthy of attention and investigation to assess therapeutic response.

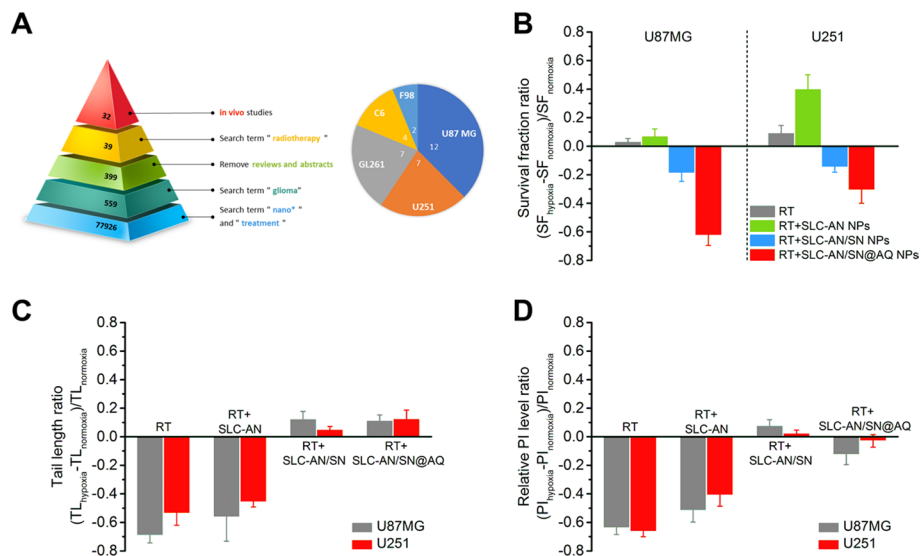


Fig. 3 Therapeutic response of the two most common GBM cell lines U87MG and U251 to low-dose pleiotropic hypoxic radiosensitive nanoformulation. **A** The illustration shows journal articles searched from the Web of Science in the last 3 years (2020–2022) to identify cell lines for nanoparticle-based RT of GBM. **B–D** The difference between U87 MG and U251 cells on this multi-effect synergistic effect of SLC-AN/SN@AQ NPs under radiation was evaluated by the following ratios calculated under normoxic and hypoxic conditions, including **B** survival fraction (SF) using colony formation assay, **C** potential DNA damage represented by tail length (TL) using the comet assay, and **D** cell death represented by relative PI level using Calcein-AM/PI dual staining

Based on the excellent multi-effect synergistic effect by SLC-AN/SN@AQ NPs shown above in U87MG cells, we further observed this therapeutic response in U251 cells. The differences between U87 MG and U251 cells were analyzed by evaluating survival fractions (SF) using colony formation assay, potential DNA damage represented by tail length (TL) using the comet assay, and cell death represented by relative PI level using Calcein-AM/PI dual staining. The ratios of SF (Fig. 3B), TL (Fig. 3C), and relative PI level (Fig. 3D) between hypoxic and normoxic U87MG and U251 cells showed the same trend in different treatment groups. Both low-dose RT and RT + SLC-AN NPs groups showed positive values of SF ratios and negative values of TL ratios and relative PI level ratios, indicating uncontrollable cell proliferation under hypoxia. In contrast, RT + SLC-AN/SN NPs and RT + SLC-AN/SN@AQ NPs groups exhibited progressively decreasing negative values of SF ratios, while the values of TL ratios and relative PI level ratios tended to be positive, representing the significantly enhanced hypoxic sensitization effect. It was noted that the therapeutic response of U251 cells was slightly weaker than that of U87MG cells, but also showed good efficacy. These results provided preliminary evidence that SLC-AN/SN@AQ NPs could exert similar therapeutic responses against different GBM cell lines.

BBB transport and brain targeting in vitro and in vivo

In order to verify the transport efficacy of ANG-modified NPs across BBB, the compact monolayers of mouse brain endothelial cells (bEnd.3) were used as an in vitro BBB model for transwell migration assay (Liu et al. 2020). TEER values measured before and after different treatments were all above $150 \Omega \cdot \text{cm}^2$ (Additional file 1: Fig. S6), indicating the integrity of the bEnd.3 cell monolayer during the experiments and the successful construction of in vitro BBB model. After NP treatments, Ln content in the cells of the lower layer was measured by ICP-OES to analyze the penetration percentage of NPs through in vitro BBB model. Without ANG modification, only 3.6% of SLC-SN@AQ NPs penetrated through the BBB layer. Remarkably, the penetration percentage of SLC-AN/SN@AQ NPs was detected to be 16.7%, which was much higher than that of ANG-unmodified NPs (Fig. 4A). To further verify ANG-mediated transcytosis, excess free ANG was added before NP treatment, and the penetration percentage of SLC-AN/SN@AQ NPs was significantly reduced to 8.6% (Fig. 4A). This phenomenon suggested that free ANG pretreatment has bound a large number of LRP receptors on the BBB, thereby preventing subsequent ANG-mediated NP transport. These results demonstrated that this nanoformulation could efficiently cross the BBB thanks to ANG surface modification.

The in vivo BBB-targeting efficacy was evaluated by detecting the temporal concentrations of Ln content in the plasma and brain of the glioma-bearing mice intravenously injected with SLC-AN/SN@AQ NPs, compared to SLC-SN@AQ NPs without ANG modification (Fig. 4B). It was found that the plasma concentration of ANG-containing NPs decayed much more slowly over time than that of ANG-free NPs, suggesting that ANG conferred a longer circulating half-life on this nanoformulation. Notably, the administration of ANG-containing NPs resulted in significantly elevated Ln levels in the brain compared to ANG-free NPs. Mice treated with ANG-free NPs had barely detectable Ln concentrations in the brain within 48 h after injection. In sharp contrast, brain Ln content was 13.5-fold higher in mice treated with ANG-containing NPs than in mice

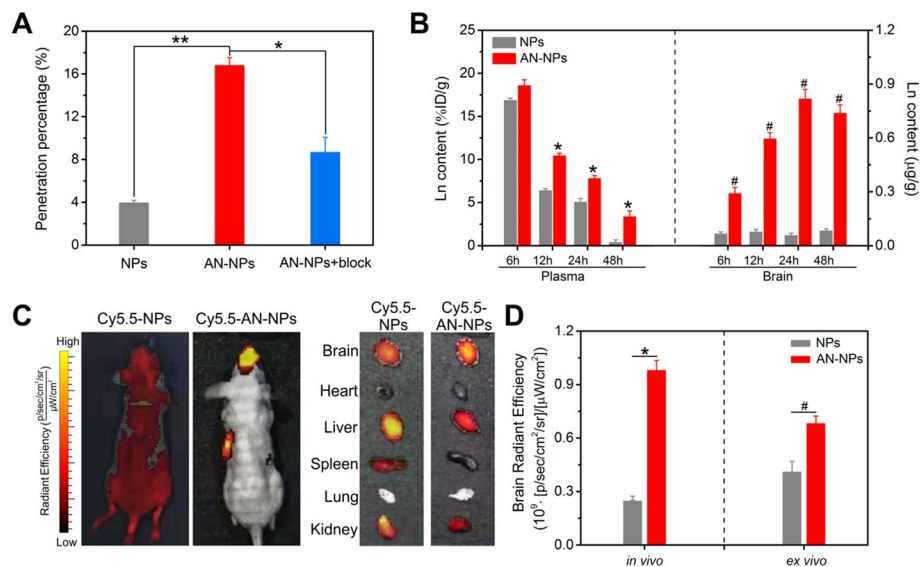


Fig. 4 BBB transport and brain targeting in vitro and in vivo. **A** Penetration percentage of SLC-SN@AQ NPs and SLC-AN/SN@AQ NPs through in vitro BBB model. Free ANG pretreatment was used as blocking. **B** Ln content in the plasma and brain of the glioma-bearing mice determined by ICP-OES after intravenous injection of NPs with and without ANG modification. **C** Fluorescence images of the living glioma-bearing mice and their ex vivo tissues at 24 h post-injection of Cy5.5-labeled NPs with and without ANG modification. **D** Quantitative analysis of fluorescence intensity in brains in **(C)**

treated with ANG-free NPs at 24 h post-injection and remained relatively high at 48 h post-injection (Fig. 4B).

Then, the in vivo fluorescence imaging of the glioma-bearing mice was performed 24 h after intravenous administration of Cy5.5-labeled SLC-AN/SN@AQ NPs, compared with Cy5.5-labeled SLC-SN@AQ NPs (Fig. 4C). As expected, the brain fluorescence intensity of mice treated with ANG-containing NPs was 3.7-fold higher than that of mice treated with ANG-free NPs (Fig. 4D). Similar phenomenon was also observed in the ex vivo fluorescence images of the resected brain tissues (Fig. 4C), confirming ANG-mediated BBB crossing. As shown in the ex vivo fluorescence images of other organs, mice treated with ANG-free NPs showed more pronounced accumulation in the liver and kidney than ANG-containing NPs-treated mice (Fig. 4C), which was also observed by measuring Ln content in these organs (Additional file 1: Fig. S7). These results demonstrated that ANG could facilitate the preferential accumulation of this nanoformulation in glioma-bearing brains and avoid its rapid clearance by the mononuclear phagocytosis system and renal metabolism.

BOLD/DWI monitoring in vivo

Based on the excellent brain-targeting ability, SLC-AN/SN@AQ NPs were intravenously administered to the glioma-bearing mice, followed by low-dose RT at 24 h post-injection. In vivo 9.4 T BOLD/DWI was applied for noninvasive efficacy monitoring before and after treatment (Fig. 5A). T2-weighted images were first used to localize glioma regions in the brain as ROIs, and then BOLD/DWI signal pseudo-color maps were obtained to quantify T2* and ADC values in glioma ROIs. The tumor volumes calculated from the T2 images showed rampant tumor growth in the control and low-dose RT

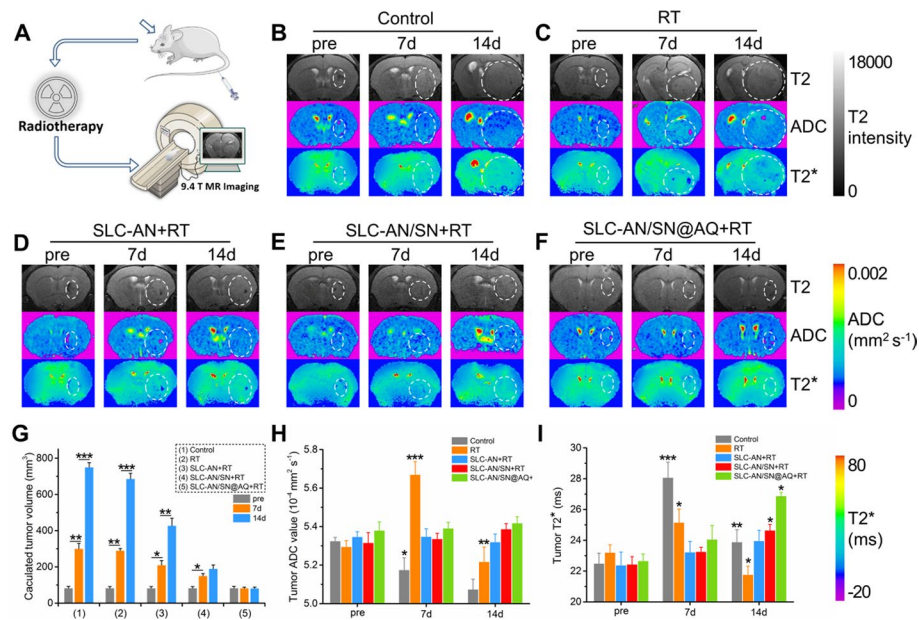


Fig. 5 BOLD/DWI monitoring in vivo. **A** Schematic diagram of treatment and imaging. **B–F** T2-weighted, ADC-mapping, and T2*-mapping whole-brain images for various treatments. **G** Imaging calculated glioma volume. **H** Glioma ADC value analysis. **I** Glioma T2* value analysis

groups. The sequential introduction of radiosensitive therapeutic components resulted in the continuous shrinking of tumor volume, among which the tumor size in the SLC-AN/SN@AQ NPs + RT group was the smallest and remained almost unchanged compared with that before treatment (Fig. 5B–G), showing a very encouraging brain glioma inhibition.

Compared with the decreasing ADC values of the control group over time (Fig. 5B), the ADC values of the RT group first increased at 7 days after treatment and then decreased at 14 days after treatment (Fig. 5C, H), indicating that low-dose radiation was not enough to completely kill tumor cells and will cause recurrence (Ni et al. 2018). The ADC values of the SLC-AN NPs + RT group did not differ much before and after treatment (Fig. 5D), indicating its limited in vivo radiosensitive effect. Both SLC-AN/SN NPs + RT and SLC-AN/SN@AQ NPs + RT groups showed a slight gradual increase in the ADC values (Fig. 5E, F), and the latter exhibited the highest ADC value at 14 days after treatment (Fig. 5H), corresponding to a very small tumor size shown by T2-weighted images. These results suggested that DWI could monitor the radiosensitivity and efficacy of brain glioma therapy in vivo by detecting ADC values that are sensitive to changes in tumor density.

The T2* values in the control group showed a first increase and then a decrease with time (Fig. 5B, I), indicating that the microvessels gradually established with tumor growth tend to be damaged and cause hypoxia. The overall level of T2* values after RT alone treatment was lower than that of the control group (Fig. 5C, I), indicating that low-dose X-rays would further damage blood vessels and reduce local blood oxygen. With the sequential introduction of radiosensitive therapeutic components, the T2* values continued to increase over time after treatment (Fig. 5D–F), indicating a

significantly improved oxygen supply to gliomas. SLC-AN/SN@AQ NPs + RT group exhibited stronger hypoxia alleviation than the SLC-AN/SN NPs + RT group (Fig. 5I), which might be because the reduced tumor density caused by AQ4N selective hypoxic killing facilitated the infiltration of large amounts of NO released under radiation into solid gliomas. The above results suggested that BOLD imaging is an effective means to monitor oxygen supply inside brain gliomas and to provide more adequate support for in vivo accurate efficacy assessment.

Evaluation of synergistic anti-glioma efficacy in vivo

To objectively assess the synergistic anti-glioma efficacy of SLC-AN/SN@AQ NPs under low-dose RT, the intact brain tissues of mice in all groups were dissected 14 days after treatment. H&E staining of whole brain sections demonstrated a very pronounced stepwise suppression of glioma size with the sequential introduction of radiosensitive therapeutic components (Fig. 6A), consistent with MRI results (Fig. 5B–G). Magnified H&E images and TUNEL staining showed substantial necrosis and apoptosis of glioma cells in the SLC-AN/SN@AQ NPs + RT group, which was slightly more than that in SLC-AN/SN NPs + RT group, but significantly more than that in other three groups (Fig. 6A), indicating the remarkable killing effect of brain gliomas by this nanoformulation.

After orthotopic implantation of brain gliomas, the body weight and survival of mice were observed until all mice died. The body weights of mice in the control group and RT alone group all decreased significantly, with little difference from each other (Fig. 6B). All studied NP treatment showed significant improvement in body weight, among which the last mice in SLC-AN/SN@AQ NPs + RT group maintained a relatively normal body weight before dying (Fig. 6B). Kaplan–Meier survival curve showed that the median survival rates of mice in the control group (21 d) and RT group (23 d) were similar and slightly higher in SLC-AN NPs + RT group (28 d) (Fig. 6C). These rapid deaths were attributed to the failure of low-dose RT and physical radiosensitization alone to suppress the rapid proliferation and invasion of gliomas (Brighi et al. 2020; Lam et al. 2018). However, the survival rates of mice in the SLC-AN/SN NPs + RT group and SLC-AN/SN@AQ NPs + RT group were significantly improved to a median of 37 and 46 days, respectively, much longer than the other treatments (Fig. 6C). The significance results of this Kaplan–Meier survival analysis are shown in Additional file 1: Table S1. These results suggested that this nanoformulation-mediated synergistic therapy could effectively improve the quality of life of glioma-bearing mice.

Furthermore, immunohistochemical staining was performed to analyze the changes of HIF1 α , p53, VEGF, and MMP-2 levels in glioma areas of brain sections to reveal the underlying mechanism preliminarily. As a hypoxia-activated important transcription factor (Wu et al. 2017), HIF1 α (hypoxia inducible factor-1) was highly expressed in the control and RT groups, slightly down-regulated in SLC-AN NPs + RT group, and significantly down-regulated in SLC-AN/SN NPs + RT group and SLC-AN/SN@AQ NPs + RT group (Fig. 6D), further validating the effective hypoxia relief in brain gliomas. In contrast to HIF1 α down-regulation, p53, an indicator of apoptosis (Yang et al. 2014), was most significantly up-regulated in SLC-AN/SN@AQ NPs + RT group, further

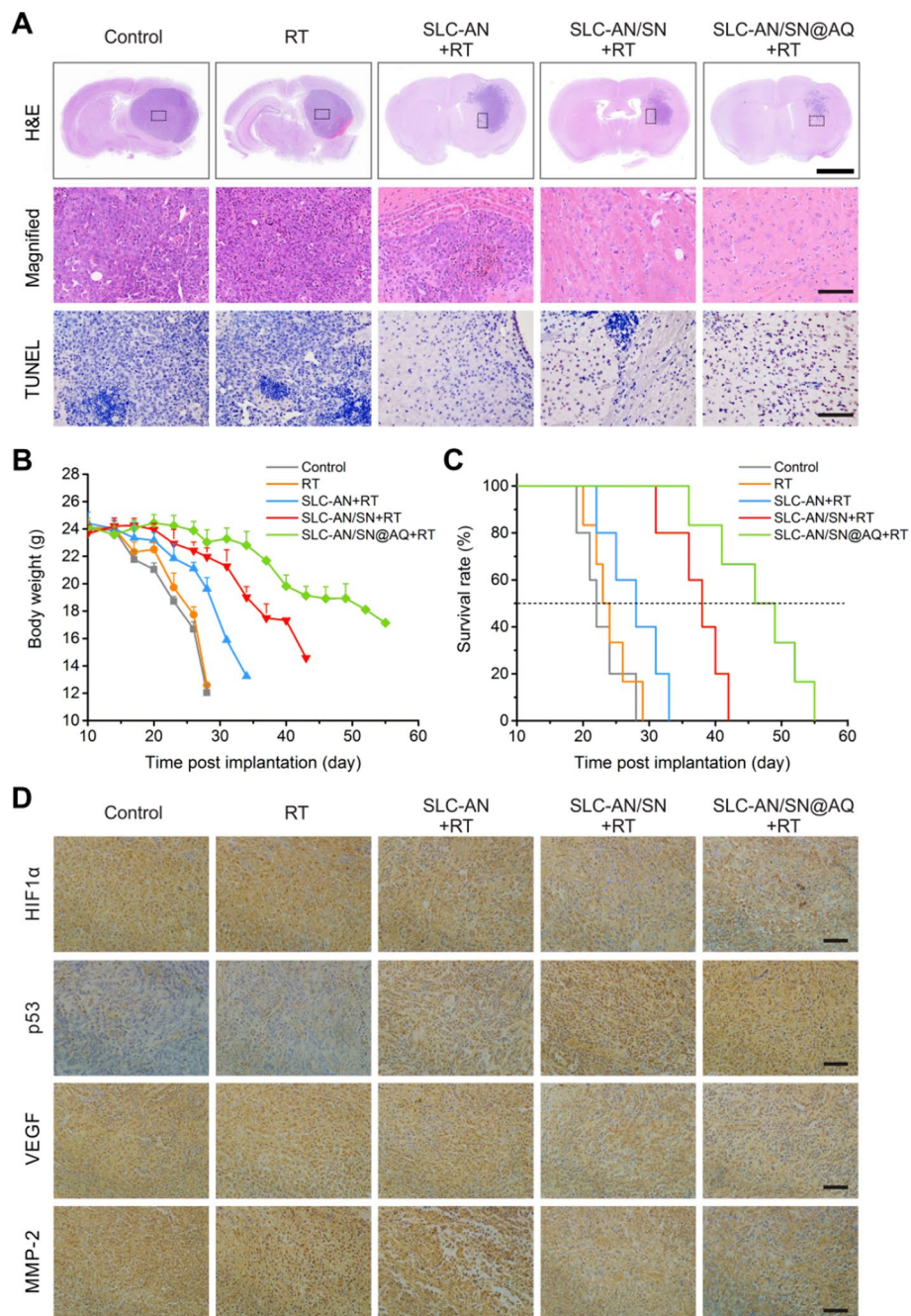


Fig. 6 Evaluation of synergistic anti-glioma efficacy in vivo. **A** Whole-brain H&E staining images (Scale bar = 200 μm) with magnified observation (Scale bar = 100 μm) and TUNEL staining images (Scale bar = 100 μm). **B** Body weight curves. **C** Survival rates. **D** Immunohistochemical staining images of p53, HIF1α, VEGF, and MMP-2 of the tumor areas in the brains of the glioma-bearing mice (Scale bar = 100 μm)

confirming the superior synergistic anti-glioma efficacy of this nanoformulation under low-dose RT. In addition, SLC-AN/SN@AQ NPs + RT group showed the lowest levels of vascular endothelial growth factor (VEGF) and matrix metalloproteinase-2 (MMP-2) (Fig. 6D), suggesting that this nanoformulation has the potential to inhibit glioma vascular angiogenesis and migration (Hu et al. 2017; Wang et al. 2019; Zeng et al. 2021).

In vivo biosafety analysis

To investigate the potential tissue toxicity of this nanoformulation, the brains and major organs of the glioma-bearing mice were collected 14 days after intravenous injection and 14 days after treatment with SLC-AN/SN@AQ NPs, respectively. H&E staining revealed no significant histological damage in important brain regions including the brainstem, cortex, striatum, and hippocampus in the glioma-free hemisphere compared with the control group (Fig. 7A), suggesting that SLC-AN/SN@AQ NPs treatment did not cause intracerebral lesions. Meanwhile, no side effects were found in major organs including the heart, liver, spleen, lung, and kidney (Additional file 1: Fig. S8), indicating the good

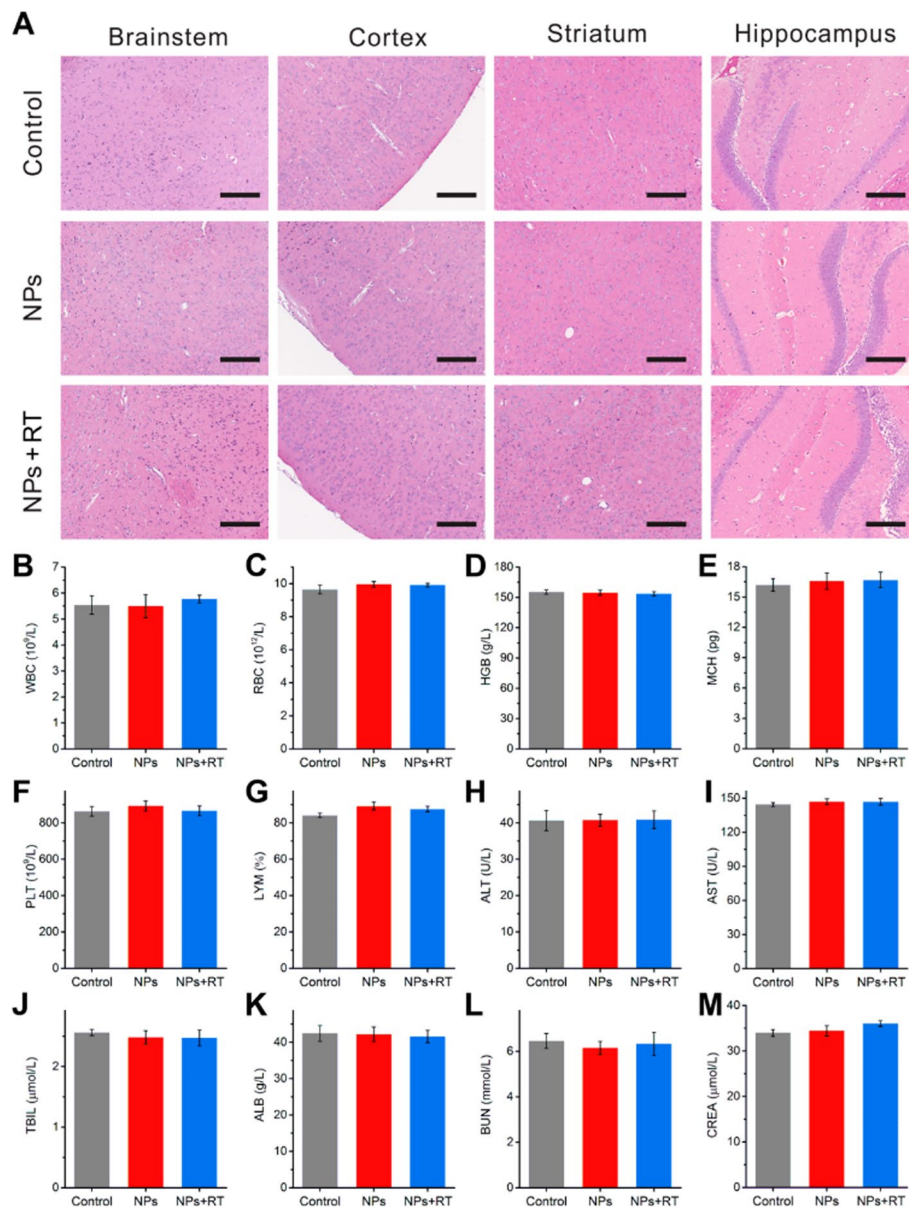


Fig. 7 In vivo biosafety analysis. **A** H&E-stained images of important brain regions from the glioma-free hemisphere in the indicated treatment groups (Scale bar = 200 μm). **B–G** Routine blood analysis: WBC, RBC, HGB, MCH, PLT, LYM. (H–M) Serum biochemistry analysis: ALT, AST, TBIL, ALB, BUN, CREA

biocompatibility of SLC-AN/SN@AQ NPs. Furthermore, the blood samples were collected for routine blood and serum biochemistry analysis. The common blood parameters, including white blood cells (WBC), red blood cells (RBC), hemoglobin (HGB), mean corpuscular hemoglobin (MCH), platelets (PLT), and lymphocytes (LYM), showed no significant changes compared to the control group (Fig. 7B–G), indicating the low hematologic toxicity. There was also no adverse impact on liver and kidney function, as indicated by normal values of related functional markers including alanine aminotransferase (ALT), aspartate aminotransferase (AST), total bilirubin (TBIL), serum albumin (ALB), blood urea nitrogen (BUN), serum creatinine (CREA) (Fig. 7H–M). Considering the prolonged lifespan and stable body weight of the glioma-bearing mice administered with this nanoformulation (Fig. 6B, C), these results preliminarily confirmed that SLC-AN/SN@AQ NPs had no appreciable biotoxicity and thus could be used as a promising radiosensitive nanoformulation for future clinical application in brain glioma treatment.

Conclusions

In summary, a low-dose pleiotropic radiosensitive nanoformulation was successfully constructed to realize the three-pronged hypoxic radiosensitization to maximize the inhibition of GBM. This nanoformulation could efficiently cross the BBB and be preferentially delivered to brain gliomas via ANG-mediated transcytosis. Both *in vitro* and *in vivo* results demonstrated that this nanoformulation exerted a synergistic therapeutic effect under low-dose radiation by combining high-Z-atom-dependent dose deposition enhancement, NO-mediated hypoxia relief, and AQ4N-induced hypoxia-activated chemotherapy to comprehensively overcome hypoxia-mediated radioresistance while extending lifespan and maintaining stable body weight in the glioma-bearing mice. More importantly, the proposed *in vivo* 9.4 T BOLD/DWI could realize real-time dynamic assessment of local oxygen supply and radiosensitivity of brain gliomas, providing sufficient *in vivo* biological information for efficacy assessment and precise prognosis of GBM. Given the potential inhibition of tumor metastasis and invasion as well as good biocompatibility, this hypoxia-specific low-dose nanoradiosensitizer is expected as a promising candidate for comprehensive treatment, noninvasive monitoring, and precise prognosis in GBM and other malignant tumors. In the future, *bona fide in vitro* and *in vivo* models such as three-dimensional glioma cell models, patient-derived glioma cell culture, and tissue transplantation animal models are expected to provide further insights into the therapeutic effects of this low-dose pleiotropic radiosensitive nanoformulation, which will help to overcome the therapeutic differences caused by the heterogeneity of brain gliomas and optimize individualized therapy of GBM.

Supplementary Information

The online version contains supplementary material available at <https://doi.org/10.1186/s12645-023-00159-w>.

Additional file 1: Figure S1. Schematic diagram of the synthesis of SLC-AN/SN@AQ NPs. **Figure S2.** BCA standard curve. **Figure S3.** Size stability of SLC-AN/SN@AQ NPs incubated in different biological media for 14 days. **Figure S4.** Cytotoxicity of SLC-AN NPs, SLC-AN/SN NPs, and SLC-AN/SN@AQ NPs to U87MG cells under normoxic or hypoxic conditions. **Figure S5.** NO production in U87MG cells after various treatments under normoxic conditions. **Figure S6.** TEER values of the bEnd.3 cell monolayer before and after different treatments. **Figure S7.** The biodistribution of SLC-SN@AQ NPs and SLC-AN/SN@AQ NPs at 24 h post-injection. **Figure S8.** Representative H&E staining of major organs in mice 14 days after SLC-AN/SN@AQ NP administration and after SLC-AN/SN@AQ NP+RT treatment, respectively. Scale bar: 100 μ m. **Table S1.** The significant results of Kaplan–Meier survival analysis in Fig. 6C.

Acknowledgements

This work was supported by Tianjin Key Medical Discipline (Specialty) Construction Project (TJYXZDXK-001A).

Author contributions

FZ and YD designed and conceptualized this study. FZ, XW, WZ, and YG performed most of the in vitro and in vivo experiments. DZ and CY helped with in vivo imaging experiments. FZ, XW, WZ, and YG analyzed the data. FZ, XW, and YD wrote the manuscript. All authors read and approved the final manuscript.

Funding

This work was funded by the Tianjin Natural Science Foundation (21JCQNJC01570), the National Natural Science Foundation of China (81801828), and The Second Hospital of Tianjin Medical University Youth Research Fund Project (2020ydey27).

Availability of data and materials

The data and materials that support the findings of this study are available from the corresponding author upon reasonable request.

Declarations

Ethics approval and consent to participate

All animal experiments were approved by the Animal Ethics Committee of Tianjin Medical University (Number IACUC E2015093).

Consent for publication

Not applicable.

Competing interests

The authors declare no competing interests.

Received: 29 September 2022 Accepted: 22 January 2023

Published online: 04 February 2023

References

- Bar EE, Lin A, Mahairaki V, Matsui W, Eberhart CG (2010) Hypoxia increases the expression of stem-cell markers and promotes clonogenicity in glioblastoma neurospheres. *Am J Pathol* 177(3):1491–1502
- Brighi C, Reid L, Genovesi LA, Kojic M, Millar A, Bruce Z et al (2020) Comparative study of preclinical mouse models of high-grade glioma for nanomedicine research: the importance of reproducing blood-brain barrier heterogeneity. *Theranostics* 10(14):6361–6371
- Bulin AL, Broekgaarden M, Chaput F, Baisamy V, Garrevoet J, Busser B et al (2020) Radiation dose-enhancement is a potent radiotherapeutic effect of rare-earth composite Nanoscintillators in preclinical models of Glioblastoma. *Adv Sci* 7(20):2001675
- Calli C, Kitis O, Yunten N, Yurtseven T, Islekel S, Akalin T (2006) Perfusion and diffusion MR imaging in enhancing malignant cerebral tumors. *Eur J Radiol* 58(3):394–403
- Cao YF, Liu MS, Cheng J, Yin JJ, Huang CS, Cui HY et al (2020) Acidity-triggered tumor-targeted nanosystem for synergistic therapy via a cascade of ROS generation and NO release. *ACS Appl Mater Interfaces* 12(26):28975–28984
- Chedeville AL, Madureira PA (2021) The Role of hypoxia in glioblastoma radiotherapy resistance. *Cancers (basel)* 13(3):542
- Choi J, Kim G, Cho SB, Im HJ (2020) Radiosensitizing high-Z metal nanoparticles for enhanced radiotherapy of glioblastoma multiforme. *J Nanobiotechnol* 18(1):122
- Compter I, Peerlings J, Eekers DBP, Postma AA, Ivanov D, Wiggins CJ et al (2016) Technical feasibility of integrating 7 T anatomical MRI in image-guided radiotherapy of glioblastoma: a preparatory study. *Magn Reson Mater Phys* 29(3):591–603
- Daruwalla J, Christophi C (2006) The effect of hyperbaric oxygen therapy on tumour growth in a mouse model of colorectal cancer liver metastases. *Eur J Cancer* 42(18):3304–3311
- De Stasio G, Rajesh D, Ford JM, Daniels M, Erhardt R, Frazer BH et al (2006) Motexafin-gadolinium taken up in vitro by at least 90% of glioblastoma cell nuclei. *Clin Cancer Res* 12(1):206–213
- Dong CY, Hong S, Zheng DW, Huang QX, Liu FS, Zhong ZL et al (2021) Multifunctionalized Gold Sub-Nanometer Particles for Sensitizing Radiotherapy against Glioblastoma. *Small* 17(5):2006582
- Du K, Xia QY, Heng H, Feng FD (2020) Temozolomide-Doxorubicin Conjugate as a double intercalating agent and delivery by Apoferritin for Glioblastoma chemotherapy. *ACS Appl Mater Interfaces* 12(31):34599–34609
- Feng LZ, Cheng L, Dong ZL, Tao DL, Barnhart TE, Cai WB et al (2017) Theranostic liposomes with HypoxiaActivated prodrug to effectively destruct hypoxic tumors post-photodynamic therapy. *ACS Nano* 11(1):927–937
- Fu JK, Li T, Yang YZ, Jiang LP, Wang WH, Fu LJ et al (2021) Activatable nanomedicine for overcoming hypoxia-induced resistance to chemotherapy and inhibiting tumor growth by inducing collaborative apoptosis and ferroptosis in solid tumors. *Biomaterials* 268:120537
- Gregory JV, Kadiyala P, Doherty R, Cadena M, Habeel S, Ruoslahti E et al (2020) Systemic brain tumor delivery of synthetic protein nanoparticles for glioblastoma therapy. *Nat Commun* 11(1):5687
- Hu Y, Li YY, Wu C, Zhou L, Han XX, Wang QY et al (2017) MicroRNA-140-5p inhibits cell proliferation and invasion by regulating VEGFA/MMP2 signaling in glioma. *Tumor Biol* 39(4):1–12

- Huang CQ, Liang JY, Ma MJ, Cheng QQ, Xu X, Zhang D et al (2020) Evaluating the treatment efficacy of nano-drug in a lung cancer model using advanced functional magnetic resonance imaging. *Front Oncol* 10:563932
- Iranmahboob A, Peck KK, Brennan NP, Karimi S, Fiscaro R, Hou B et al (2016) Vascular reactivity maps in patients with gliomas using breath-holding BOLD fMRI. *J Neuroimaging* 26(2):232–239
- Jiang Y, Yang WJ, Zhang J, Meng FH, Zhong ZY (2018) Protein toxin chaperoned by LRP-1-targeted virus-mimicking vesicles induces high-efficiency glioblastoma therapy *In vivo*. *Adv Mater* 30(30):e1800316
- Kizaka-Kondoh S, Inoue M, Harada H, Hiraoka M (2003) Tumor hypoxia: a target for selective cancer therapy. *Cancer Sci* 94(12):1021–1028
- Lam FC, Morton SW, Wyckoff J, Han TLV, Hwang MK, Maffa A et al (2018) Enhanced efficacy of combined temozolomide and bromodomain inhibitor therapy for gliomas using targeted nanoparticles. *Nat Comm* 9(9):1991
- Li SY, Sun WJ, Luo Y, Gao YP, Jiang XP, Yuan C et al (2021) Hollow PtCo alloy nanospheres as a high-Z and oxygen generating nanozyme for radiotherapy enhancement in non-small cell lung cancer. *J Mater Chem B* 9(23):4643–4653
- Liu ZC, Yan LF, Hu YC, Sun YZ, Tian Q, Nan HY et al (2017a) Combination of IMM-DWI and 3D-ASL for differentiating true progression from pseudoprogression of Glioblastoma multiforme after concurrent chemoradiotherapy: study protocol of a prospective diagnostic trial. *BMC Med Imaging* 17:10
- Liu HM, Xie YD, Zhang YF, Cai YF, Li BY, Mao HL et al (2017b) Development of a hypoxia-triggered and hypoxic radiosensitized liposome as a doxorubicin carrier to promote synergetic chemo-/radio-therapy for glioma. *Biomaterials* 121:130–143
- Liu J, Zhang YX, Chen TL, Chen HJ, He HQ, Jin T et al (2020) Environmentally self-adaptative nanocarriers suppress glioma proliferation and stemness via codelivery of shCD163 and doxorubicin. *ACS Appl Mater Interfaces* 12(47):52354–52369
- Lu VM, Crawshaw-Williams F, White B, Elliot A, Hill MA, Townley HE (2019) Cytotoxicity, dose-enhancement and radiosensitization of glioblastoma cells with rare earth nanoparticles. *Artif Cell Nanomed b* 47(1):132–143
- Lu GH, Wang XJ, Li F, Wang S, Zhao JW, Wang JY et al (2022) Engineered biomimetic nanoparticles achieve targeted delivery and efficient metabolism-based synergistic therapy against glioblastoma. *Nat Commun* 13(1):4214
- Ni KY, Lan GX, Veroneau SS, Duan XP, Song Y, Lin WB (2018) Nanoscale metal-organic frameworks for mitochondria-targeted radiotherapy-radiodynamic therapy. *Nat Commun* 9:4321
- Omuro A, DeAngelis LM (2013) Glioblastoma and other Malignant Gliomas a clinical review. *J Am Med Assoc* 310(17):1842–1850
- Shen SH, Wu YS, Li K, Wang Y, Wu JM, Zeng Y et al (2018) Versatile hyaluronic acid modified AQ4N-Cu(II)-gossypol infinite coordination polymer nanoparticles: multiple tumor targeting, highly efficient synergistic chemotherapy, and real-time self-monitoring. *Biomaterials* 154:197–212
- Shen ZY, Liu T, Yang Z, Zhou ZJ, Tang W, Fan WP et al (2020) Small-sized gadolinium oxide based nanoparticles for high-efficiency theranostics of orthotopic glioblastoma. *Biomaterials* 235:119783
- Shi Y, Jiang J, Cui YZ, Chen YD, Dong TX, An HD et al (2021) MSH6 aggravates the hypoxic microenvironment via regulating HIF1A to promote the metastasis of Glioblastoma Multiforme. *DNA Cell Biol* 40(1):93–100
- Song XJ, Feng LZ, Liang C, Yang K, Liu Z (2016) Ultrasound triggered tumor oxygenation with oxygen-shuttle nanoperofluorocarbon to overcome hypoxia-associated resistance in cancer therapies. *Nano Lett* 16(10):6145–6153
- Song GS, Cheng L, Chao Y, Yang K, Liu Z (2017) Emerging nanotechnology and advanced materials for cancer radiation therapy. *Adv Mater* 29(32):170096
- Sung YC, Jin PR, Chu LA, Hsu FF, Wang MR, Chang CC et al (2019) Delivery of nitric oxide with a nanocarrier promotes tumour vessel normalization and potentiates anti-cancer therapies. *Nat Nanotechnol* 14(12):1160–1169
- Tan AC, Ashley DM, Lopez GY, Malinzak M, Friedman HS, Khasraw M (2020a) Management of glioblastoma: State of the art and future directions. *CA Cancer J Clin* 70(4):299–312
- Tan JY, Duan XH, Zhang F, Ban XH, Mao JJ, Cao MH et al (2020b) Theranostic nanomedicine for synergistic chemodynamic therapy and chemotherapy of Orthotopic Glioma. *Adv Sci* 7(24):2003036
- Tian XH, Nyberg S, Sharp PS, Madsen J, Daneshpour N, Armes SP et al (2015) LRP-1-mediated intracellular antibody delivery to the central nervous system. *Sci Rep* 5:11990
- Toth V, Forschler A, Hirsch NM, den Hollander J, Kooijman H, Gempt J et al (2013) MR-based hypoxia measures in human glioma. *J Neurooncol* 115(2):197–207
- Wang YS, Tan XR, Li S, Yang SL (2019) The total flavonoid of *Eucommia ulmoides* sensitizes human glioblastoma cells to radiotherapy via HIF- α /MMP-2 pathway and activates intrinsic apoptosis pathway. *Onco Targets Ther* 12:5515–5524
- Wang CJ, Liang C, Hao Y, Dong ZL, Zhu YJ, Li QG et al (2021) Photodynamic creation of artificial tumor microenvironments to collectively facilitate hypoxia-activated chemotherapy delivered by coagulation-targeting liposomes. *Chem Eng J* 414:128731
- Wen PY, Weller M, Lee EQ, Alexander BM, Barnholtz-Sloan JS, Barthel FP et al (2020) Glioblastoma in adults: a society for neuro-oncology (SNO) and European Society of Neuro-Oncology (EANO) consensus review on current management and future directions. *Neuro Oncol* 22(8):1073–1113
- Wu W, Hu Q, Nie E, Yu T, Wu Y, Zhi T et al (2017) Hypoxia induces H19 expression through direct and indirect Hif-1 α activity, promoting oncogenic effects in glioblastoma. *Sci Rep* 7:45029
- Xie T, Chen X, Fang JQ, Xue W, Zhang JF, Tong HP et al (2021) Non-invasive monitoring of the kinetic infiltration and therapeutic efficacy of nanoparticle-labeled chimeric antigen receptor T cells in glioblastoma via 7.0-Tesla magnetic resonance imaging. *Cytotherapy* 23(3):211–222
- Xu Y, Liu JW, Liu ZY, Ren H, Yong JH, Li WL et al (2020) Blockade of platelets using tumor-specific NO-releasing nanoparticles prevents tumor metastasis and reverses tumor immunosuppression. *ACS Nano* 14(8):9780–9795
- Yang SH, Wang SM, Syu JP, Chen Y, Wang SD, Peng YS et al (2014) Andrographolide induces apoptosis of C6 glioma cells via the ERK-p53-caspase 7-PARP pathway. *Biomed Res Int* 2014:312847
- Zeng WH, Wu LY, Sun YD, Wang YQ, Wang JF, Ye DJ (2021) Ratiometric imaging of MMP-2 activity facilitates tumor detection using activatable near-infrared fluorescent semiconducting polymer nanoparticles. *Small* 17(36):2101924
- Zhang FM, Liu SK, Zhang N, Kuang Y, Li WT, Gai SL et al (2020) X-ray-triggered NO-released Bi-SNO nanoparticles: all-in-one nano-radiosensitizer with photothermal/gas therapy for enhanced radiotherapy. *Nanoscale* 12(37):19293–19307

- Zhang J, Chen C, Li AN, Jing WQ, Sun P, Huang XY et al (2021) Immunostimulant hydrogel for the inhibition of malignant glioma relapse post-resection. *Nat Nanotechnol* 16(5):538–548
- Zhou W, Liu ZL, Wang NN, Chen X, Sun XZ, Cheng YF (2022) Hafnium-based metal-organic framework nanoparticles as a radiosensitizer to improve radiotherapy efficacy in Esophageal cancer. *ACS Omega* 7(14):12021–12029
- Zou MZ, Liu WL, Chen HS, Bai XF, Gao F, Ye JJ et al (2021) Advances in nanomaterials for treatment of hypoxic tumor. *Natl Sci Rev* 8(2):nwaa160

Publisher's Note

Springer Nature remains neutral with regard to jurisdictional claims in published maps and institutional affiliations.

Ready to submit your research? Choose BMC and benefit from:

- fast, convenient online submission
- thorough peer review by experienced researchers in your field
- rapid publication on acceptance
- support for research data, including large and complex data types
- gold Open Access which fosters wider collaboration and increased citations
- maximum visibility for your research: over 100M website views per year

At BMC, research is always in progress.

Learn more biomedcentral.com/submissions

